ACCURATE TOP OF THE ATMOSPHERE ALBEDO DETERMINATION FROM MULTIPLE VIEWS OF THE MISR INSTRUMENT

Christoph C. Borel, Siegfried A. W. Gerstl
NIS-2, Mailstop C323, Los Alamos National Laboratory, Los Alamos, NM 87545, USA
Carmen Tornow
German Aerospace Research Establishment, Rudower Chaussee, 12484 Berlin, Germany

March 29, 1996

ABSTRACT

Changes in the Earth's surface albedo impact the atmospheric and global energy budget and contribute to global climate change. It is now recognized that multi-spectral and multi-angular views of the Earth's top of the atmosphere (TOA) albedo are necessary to provide information on albedo changes. In this paper we describe four semi-empirical bidirectional reflectance factor (BRF) models which are inverted for two and three unknowns. The retrieved BRF parameters are then used to compute the TOA spectral albedo for clear sky conditions. Using this approach we find that the albedo can be computed with better than 1% error in the visible and 1.5% in the near infrared (NIR) for most surface types.

Keywords : **Top of atmosphere albedo, MISR, EOS, Radiative Transfer**

1 Introduction

The Multi-angle Imaging Spectro-Radiometer (MISR) instrument is slated for the EOS-AM platform to be launched in 1998. The instrument consists of nine cameras pointed at zenith angles of ± 70.5, ± 60, ± 45, ± 26.1 and 0 degrees in the along track direction. Each camera has four spectral channels with center bandpass wavelengths at 443 nm (blue), 550 nm (green), 670 nm (red) and 865 nm (near infrared). The instrument will be used to infer top of the atmosphere spectral albedo (clear and cloudy conditions), surface bidirectional reflectance, global aerosol distributions and other atmosphere and surface parameters at the 4 spectral bands.

Global monitoring of the earth radiation budget is one of the main goals in global change research programs. Thus global measurements of the TOA albedo are important (Kimes and Sellers, 1985, Li et al ., 1993). Our goal is to compute the TOA spectral albedo for clear sky conditions from MISR measurements (Diner et al., 1994).

1.1 Definition of TOA Albedo

The albedo in each MISR channel c, $c = [1, 2, 3, 4]$ is defined according to Nicodemus et al, 1977, as:

$$\alpha_{0,c}(\mu_s) \;=\; \frac{1}{\pi} \int_0^1 d\mu_v \mu_v \int_0^{2\pi} d\phi_v \; BRF_c(\mu_s,\, \mu_v, \phi_v), \tag{1}$$

with the notation:

$\alpha_{0,c}(\mu_s)$ is the top of atmosphere albedo in MISR channel c,

ϕ_v is the angle relative to the solar azimuth,

μ_s is the cosine of the solar zenith angle θ_0,

μ_v is the cosine of the view zenith angle θ and

$BRF_c(\mu_s,\, \mu_v,\, \phi_v)$ is the bidirectional reflectance factor in MISR channel c.

The relationship between the BRF and the bidirectional reflectance distribution function $BRDF$ is

$$BRDF_c(\mu_s, \mu_v, \phi_v) \;=\; \frac{1}{\pi}\, BRF_c(\mu_s, \mu_v, \phi_v). \tag{2}$$

The BRF_c is related to the radiance L_c by the following equation

$$BRF_c(\mu_s, \mu_v, \phi_v) \;=\; \frac{\pi\; L_c(\mu_s, \mu_v, \phi_v)\; D^2}{\mu_s\; E_{0,c}}, \tag{3}$$

where $D = R(t)/R_0$ is the normalized distance to the sun. $R(t)$ is the time dependent distance and R_0 is the distance for which E_0 is defined and E_0 is the TOA solar irradiance.

For each channel MISR, has nine cameras that measure the BRF at nadir and at four different off nadir zenith in two different azimuthal angles (forward and aft). Since we have only two azimuthal measurements for each off nadir zenith angle we need an azimuthal model to interpolate between the MISR measurements. This model has to be true for different surface cover types and for various atmospheric conditions. Thus, to find an appropriate AZM we compute the $BRF_c(\mu_s, \mu_v, \phi_v)$ and the TOA albedo $\alpha_{0,c}(\ \mu_s)$ for a number of model cases.

2 Simulated MISR Data Set

Since there is no MISR data yet available it was necessary to simulate MISR data as closely as possible to what is expected from the EOS instrument in a few years. Several "Radiative transfer" (RT) codes were considered for this task. A key requirement was that the surface had to be modeled using a surface "Bidirectional Reflectance Distribution Function" (BRDF) (e.g. Nicodemus et al, 1977). Furthermore the RT codes must accurately calculate the multiple scattering for a large range of sun and view angles in order to perform a numerical integration over the hemispherical BRF for the albedo calculation. Multiple scattering is an important component of the measured signal in the visible and near infrared spectral region. MODTRAN uses a two stream approximation to calculate the multiple scattering. However, to compute the radiance with an error less than 1% (Koepke et al., 1985) one needs at least an eight stream approximation (Li et al., 1985). Two stream approximations can cause up to 20% error (King and Harshvardhan, 1985) and thus cannot be used to model the radiative transfer for the MISR channels.

We considered and used two available codes - 6S (Vermote et al, 1994) and JMRT (Martonchik, 1994). The RT code MODTRAN3 was not used yet since it was not available prior to this work (Abreu et al, 1995).

2.1 The "John Martonchik Radiative Transfer" (JMRT) Code

Using a radiative transfer code written by John Martonchik at JPL we generated hemispherical TOA radiance fields for four MISR channels, five different aerosol types (urban, rural, maritime, desert and arctic) and 46 surface BRDF's from experimental data and models for vegetation (23), bare soil (3), rough water surface (11), snow and ice (9).

In the original JMRT output, the BRF values are given only at the MISR camera angles. In two slightly different versions we compute the BRFs for the following quadrature zenith angles : 77.00^o, 65.0^o, 52.50^o, 37.00^o, $\underline{0.00^o}$ (version 1) and 85.00^o, $\underline{70.50^o}$, $\underline{60.00^o}$, $\underline{45.60^o}$, $\underline{26.10^o}$ (version 2). Note that the underlined zenith quadrature angles are also the MISR camera zenith angles.

In addition to these changes the JMRT code is now able to read any given BRDF model directly from a modified BRDF subroutine instead of having an additional subroutine for the Kimes data only (Kimes and Sellers, 1985). Any measured BRDF can be entered as well, given that it has been measured at certain view angles and sun angles.

We have set up a driver program written in IDL to create the input parameters for JMRT and to compute TOA BRF values at the 10 zenith and at 12 relative azimuthal quadrature angles (0^o, 30^o, ... ,330^o).

Using the computed angular-dependent hemispherical data we can compute a "true" TOA albedo $\alpha_{0,c}(\mu_s)$ based on fine scale RT calculations in $N_\phi = 12$ azimuthal and $N_\theta = 10$ elevation angles:

$$\alpha_{0,c}(\mu_s) \;=\; Const\frac{2\pi}{N_\phi - 1}\sum_{i=1}^{N_\theta - 1}\mu_l \sum_{j=1}^{N_\phi - 1}\frac{\mu_i BRF_c(\mu_i,\phi_j) + \mu_{i+1}BRF_c(\mu_{i+1},\phi_j)}{2(\mu_{i+1}-\mu_i)}, \tag{4}$$

where $Const$ is determined by setting $\alpha_0(\mu_s) = 1$ with $BRF_c(\mu_v,\phi_v) = 1$ in eq.(4). Equation (4) is called a 1-step Newton-Cotes integration. We also used a 5-step integration with little difference in results. An improvement in accuracy is achieved when the BRF is first interpolated using bilinear or cubic interpolation.

3 Azimuthal Models for the Top of the Atmosphere Reflectance

3.1 Purpose of an Azimuthal Model

Since MISR measures only in nine discrete directions it is necessary to estimate the TOA radiance in directions which are not seen by MISR using what we call an azimuthal model (AZM). Various AZM's were considered in this study and used to compute an albedo estimate $\alpha_{0,c}$. We investigated an approach which summed five MISR measurements in the forward and aft directions (which included the nadir camera). The solution of two linear equations gave two resulting values which could then be used to compute the albedo. A similar approach was used to compute such values for each MISR camera in the forward and aft direction and then the albedo. While this approach worked quite well and described in the MISR ATBD document (http://spso.gsfc.nasa.gov/atbd/misr/atbdmisr03.html) and internal LANL reports (Borel, Tornow and Gerstl, 1995; Tornow, Borel and Gerstl, 1995) it will not be considered further here. Instead another approach which seems quite promising will be taken . A semi-empirical function which is able to represent many different TOA BRFs is used. This function has as few parameters as possible, be uniquely invertible and reciprocal (sun and view angles are interchangeable without changing the value) and has little sensitivity to noise.

3.2 The Coupled Surface-Atmosphere Reflectance (CSAR) Model

There are quite a few semi-empirical BRFs reported in the literature (Goel, 1988) but only some of them are reciprocal. As a starting point we decided to investigate the "Coupled Surface-Atmosphere Reflectance" (CSAR) model further. In Rahman et al., 1993 the following semi-empirical model is suggested to model BRFs of terrestrial surfaces:

$$BRF_{CSAR}(\theta_s, \phi_s; \theta_v, \phi_v) \;=\; \varrho_0 \frac{\mu_s^{\kappa-1}\mu_v^{\kappa-1}}{(\mu_s+\mu_v)^{1-\kappa}} F(g)[1+R(G)], \tag{5}$$

where ϱ_0 and κ are empirical surface parameters between 0 and 1 with the condition on ϱ_0 that the albedo of eq.(5) is between 0 and 1, and

$F(g)$ is the Henyey-Greenstein function:

$$F(g) = \frac{1-\Theta_0^2}{[1+\Theta_0^2 - 2\Theta_0\cos(\pi-g)]^{1.5}}$$

Θ_0 controls the forward ($0 \le \Theta_0 \le 1$) and backward (hot spot) ($-1 \le \Theta_0 \le 0$) scattering peak,

g is a phase angle and given by: $\cos g = \mu_s\mu_v + \sin\theta_s \sin\theta_v \cos(\phi_s - \phi_v)$,

$(1+R(G))$ approximates the hot-spot with:

$$1 + R(G) = 1 + \frac{1-\varrho_0}{1+G},$$

where $G = \sqrt{\tan^2\theta_s + \tan^2\theta_v - 2\tan\theta_s\tan\theta_v\cos(\phi_s-\phi_v)}$.

In Fig. 1 we show a polar representation of the BRF for variable Θ_0 and κ. The center of each circle represents nadir. The radial direction is given by $\sin\theta$. The principal plane (plane in which the solar vector and the surface normal lie) is along the horizontal axis with the sun position on the right side.

3.3 Uniqueness

To test whether a BRF model is invertible we wrote an IDL program to create many different BRF slices similar to MISR data using the CSAR semi-empirical function for randomly chosen parameters ϱ_0, κ and Θ_0. A non linear least squares fitting routine (CURVEFIT.PRO) was used to invert the BRF slices and compare the retrieved parameters $\widehat{\varrho_0}$, $\widehat{\kappa}$ and $\widehat{\Theta_0}$ with the original set ϱ_0, κ and Θ_0. The procedure used consists of the following steps:

1. Generate N_p randomly chosen parameters: $\varrho_{0,i}$, κ and $\Theta_{0,i}$, $i = 1, 2, 3, \ldots, N_p$.
2. Calculate N_p BRF slices $BRF(\theta_s, \phi_s; \vec{\theta_v}, \vec{\phi_v}; \varrho_{0,i},\ \kappa,\ \Theta_{0,i})$ using eq.(5).
3. Invert BRF model for $\widehat{\varrho_{0,i}}$, $\widehat{\kappa}$ and $\widehat{\Theta_{0,i}}$.
4. Compute errors $\varepsilon(\varrho_{0,i}) = \widehat{\varrho_{0,i}} - \varrho_{0,i}$, $\varepsilon(\kappa) = \widehat{\kappa} - \kappa$ and $\varepsilon(\Theta_{0,i}) = \widehat{\Theta_{0,i}} - \Theta_{0,i}$ and the "Root Mean Square Error" (RMSE) of the BRF slice difference $(\widehat{BRF_i} - BRF_i)$.

No case was observed where another solution was found. While this is not a mathematical proof that the CSAR BRF is unique, it is sufficient for our purposes.

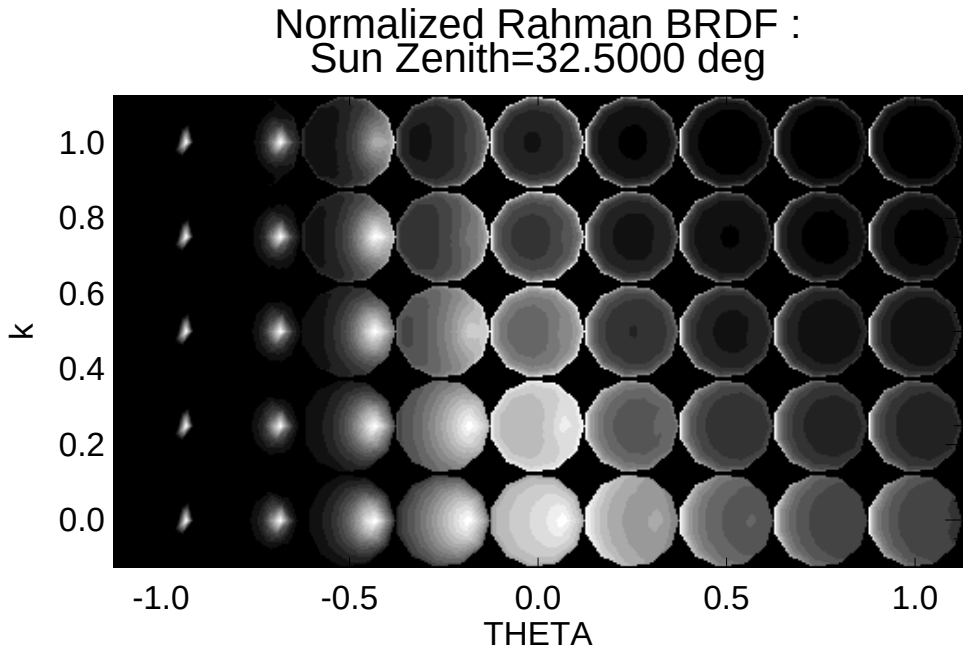

Figure 1: Polar representation of the CSAR BRF for $\theta_s = 32.5^o$ and $\varrho_0 = 0.2$ as a function of Θ_0 and κ.

3.4 Noise Sensitivity

Next we investigated how much noise could be tolerated and how the albedo error changes as a function of added noise. The following steps outline our simulation (channel index c is suppressed):

1. Generate a BRF slice BRF for a fixed set of parameters: $\theta_s = 30^o$, $\varrho_0 = 0.5$, $\kappa = 0.3$ and $\Theta_0 = 0.22$ and compute the albedo α_0 using a numerical integration technique (e.g. 1-step or 5-step Newton-Cotes integration).
2. For $i = 1, \ldots, N_p$ cases do:
   (a) $BRF_i = BRF + \sigma_i N_i(0,1)$, where $N(0,\sigma_i)$ denotes the i-th realization of a Gaussian distributed random vector with mean 0 and standard deviation σ_i where $\sigma_i = \{1,2,3,\ldots,N_p\}\Delta_\sigma$ and Δ_σ is an increment.
   (b) Retrieve the BRF parameters: $\widehat{\varrho_{0,i}}$, $\widehat{\kappa}$ and $\widehat{\Theta_{0,i}}$ and the fitted $\widehat{BRF_i}$. Compute the albedo $\widehat{\alpha_0}$ of the inverted BRF.
3. Plot the BRF, BRF_i and $\widehat{BRF_i}$ as a function of MISR camera angle.
4. Plot σ_i on the x-axis and $[(\alpha_0 - \widehat{\alpha_{0,i}}),\ (BRF - \widehat{BRF_i}),\ (\varrho_0 - \widehat{\varrho_{0,i}}),\ (\kappa - \widehat{\kappa}),\ (\Theta_0 - \widehat{\Theta_{0,i}})]$ on the y-axis.

We found that the albedo error was less than $\pm 5\%$ for $\sigma \leq 0.1$ for an albedo of 0.43. Thus there is a linear degradation of the albedo with standard deviation. Similarly the error between original and retrieved BRF parameters grows with increased noise.

4 Clear Sky Top of Atmosphere Albedo Algorithm

4.1 Algorithm Outline

The following algorithm was implemented and tested on simulated MISR BRFs over many surface types and atmospheric conditions (channel index c is suppressed):

1. Read TOA BRFs from JMRT output.
2. For all N_k cases $k = 1, 2, 3, \ldots, N_c$ do:
   (a) Compute the albedo $\alpha_{0,k}$ using Newton-Cotes integration over the quadrature angles.
   (b) For view azimuthal angles $\phi_j = [0^o,\ 30^o,\ 60^o,\ 90^o]$ do:
      i. Extract a BRF slice ($BRF_i,\ i = 1, 2, \ldots, 9$ at the MISR angles for ($\phi_j,\ \phi_j + 180^o$).
      ii. Perform nonlinear curve fit of $BRF_{j,i}$ results in estimated CSAR parameters $\widehat{\varrho_{0,j,k}}$, $\widehat{\kappa_{j,k}}$ and $\widehat{\Theta_{0,j,k}}$.
      iii. Do a numerical integration of CSAR model over the hemisphere results in estimated albedo $\widehat{\alpha_{0,j,k}}$.
      iv. Compute albedo error $\varepsilon(\alpha_{0,j,k}) = \alpha_{0,k} - \widehat{\alpha_{0,j,k}}$.
   (c) Plot standard deviation σ of the albedo error $\varepsilon(\alpha_{0,j,k})$ as a function of view azimuth ϕ_j.
   (d) Generate TOA BRF from estimated CSAR parameters and display next to original.
3. Generate scatter plots of standard deviation of the albedo error versus azimuth marking different surface types with symbols.

5 Results

Various retrieval schemes will be discussed in the next 4 sub-sections using the same TOA-BRF data set. The standard deviation σ of the albedo error was computed over all cases dividing them into general surface classes of:

$\triangle$ Vegetation (23 models),

$\diamond$ Soil and sand (3 models),

$+$ Snow and ice (9 models) and

$*$ Water (11 models),

where the plot symbols used in Figures 2-5 are shown. Note that we plot data points outside the 4% limit as symbols with an error in % in brackets. Each surface model was used in 5 different atmospheres and 3 sun angles. Thus a total of 690 TOA BRFs were inverted for 4 different azimuthal angles at (0^o, 30^o, 60^o and 90^o). Including all 4 channels this data set grows to 11040 cases. This process (with visualization of the original and fitted BRFs in polar surface plots) took several hours on a Sparc10 workstation and depended on the RMS error criterion for convergence. It is clear that the final EOS data would not be able to go through the same processing and that faster inversion routines must be found to make this approach practicable for the EOS data information system. We therefore are also trying to reduce the number of parameters in the model to less than three and including correction terms for atmospheric effects. Some of our results are reported in the next sub-sections.

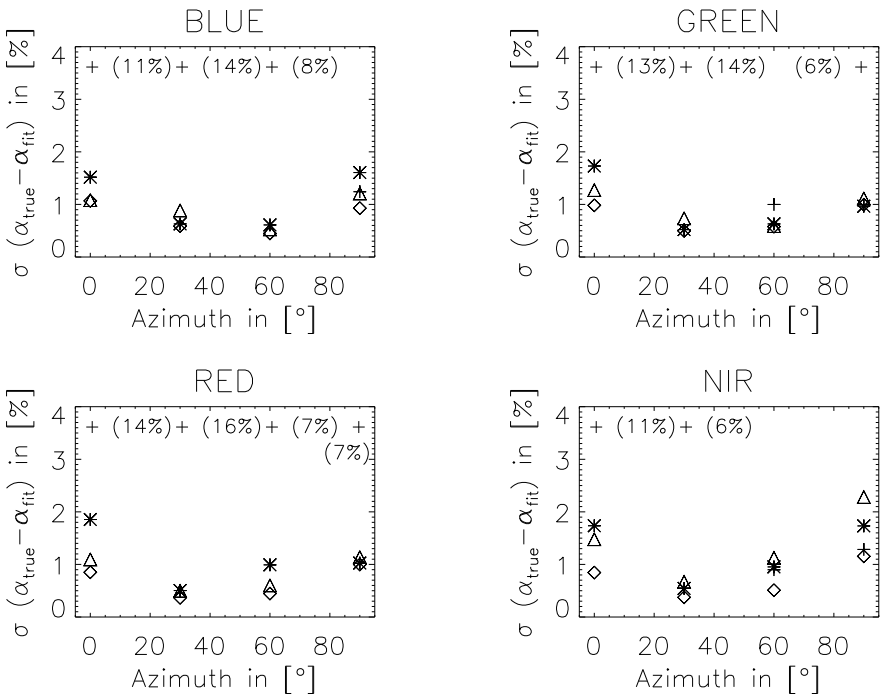

Figure 2: Standard deviation of the albedo error for the original (but with no parameter limits) CSAR BRF model as a function of surface cover (see section 5).

5.1 Algorithm using Three Parameters (no Limits) CSAR Model

First we investigated the use of the full CSAR model (with parameter limits) in section 4.1 described algorithm:

$$BRF_1(\theta_i, \phi_i) = BRF_{CSAR}(\theta_i, \phi_i; \varrho_0, \kappa, \Theta_0), i = 1, \ldots, 9 \tag{6}$$

We found that the retrieved albedos were very small for BRF slices away from the principal plane ($\phi_i = 0$, the plane defined by the surface normal and the sun vector ($\theta_s, \phi_s = 0$)) but had larger errors elsewhere. Especially for snow and ice which have larger reflectances and a more Lambertian character, the errors exceeded the 5% level for many azimuthal angles in most channels. We attributed this to the inversion routine which was not able to find a good solution in the 20 iteration limit and RMSE errors of 0.001. We noted that running the inversion without parameter limits often did not converge at all and parameters grew to infinity.

5.2 Algorithm using Two Parameters (with Limits) CSAR Model

MISR does not measure in the principle plane, therefore one may argue that a parameter which models forward or backward scattering (e.g. Θ_0 for the CSAR model) should not be used. Thus we modified the CSAR BRF and set the term $F(g)$ in eq.(5) to unity. This step improved the retrieval of the TOA albedo for bright and Lambertian surfaces which often showed erroneous hot-spots or specular peaks. In order to keep the parameters ϱ_0 and κ within their limits specified by CSAR, a variable transform from the original unbound variable ϱ_0 to the interval limited variable ϱ_0' was used:

$$\varrho_0' = \frac{1}{2} + \frac{\tan^{-1}(\varrho_0)}{\pi}$$

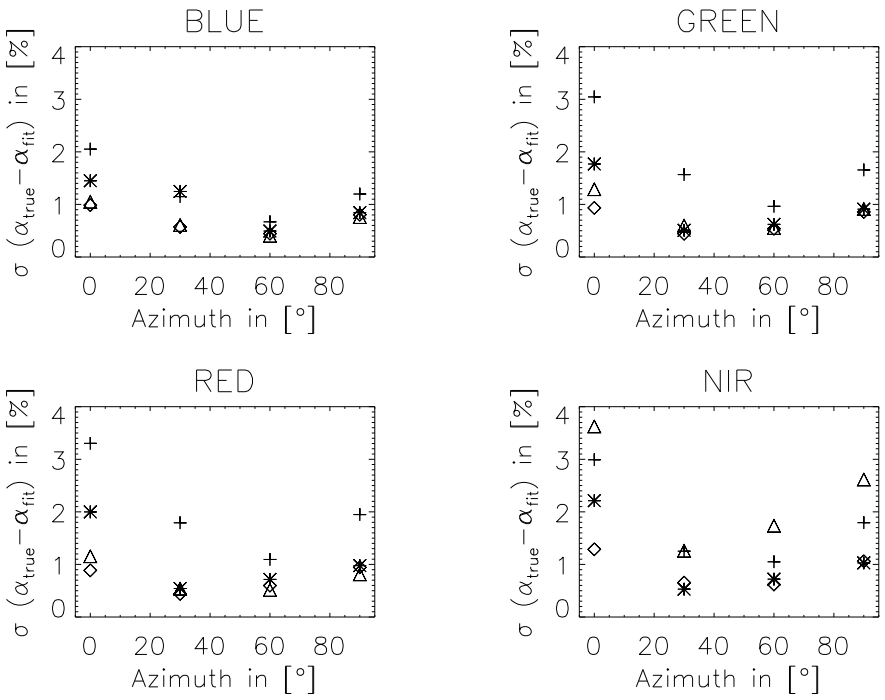

Figure 3: Standard deviation of the albedo error for a version of the parameter limited CSAR BRF without the hot spot parameter Θ. as a function of surface cover (see section 5)

and it's inverse:

$$\varrho_0 = \tan(\pi(\varrho_0 - \frac{1}{2})).$$

Similarilly κ can be transformed to κ'. The BRF used was given by:

$$BRF_2(\theta_i, \phi_i) = BRF_{CSAR}(\theta_i, \phi_i; \varrho_0', \kappa', F(g) = 1), \quad i = 1, \ldots, 9. \tag{7}$$

The result is shown in Figure 3. The method works well for all cases and channels ($\sigma < 3.8\%$) For more typical MISR azimuthal angles between 30^o and 60^o the albedo errors are below 2% which is very good.

5.3 Algorithm with Atmospheric Transmission Correction

Visualizing the resulting TOA BRF fields for the BRF_1 and BRF_2 models we noticed that the BRF near the horizon ($80^o < \theta_v < 90^o$) often was very much larger than the computed BRF from JMRT. To "correct" the CSAR model for this effect we introduced a mean transmission factor $T_c = \exp(-\tau_c/\mu_i)$ where $\tau_c = [.24, .094, .043, .015]$ and c is the channel indicator. Using this factor and an unconstrained CSAR model resulted in:

$$BRF_3(\theta_i, \phi_i) = BRF_{CSAR}(\theta_i, \phi_i; \varrho_0, \kappa, \Theta) \exp(-\tau_c/\mu_i), \quad i = 1, \ldots, 9; \; c = 1, 2, 3, 4 \tag{8}$$

The result is shown in Figure 4. Note that we meet our goal in the NIR with all surface cases. A somewhat anomalous case is in the green channel with vegetation at $\phi_i = 60^o$. Again the snow and ice surfaces cause problems in the inversion. Overall the performance is very good even for $\phi_i = 0^o$ and $\phi_i = 90^o$. It also seems that the transmission term helps in the inversion process. We did find few convergence problems for most surfaces.

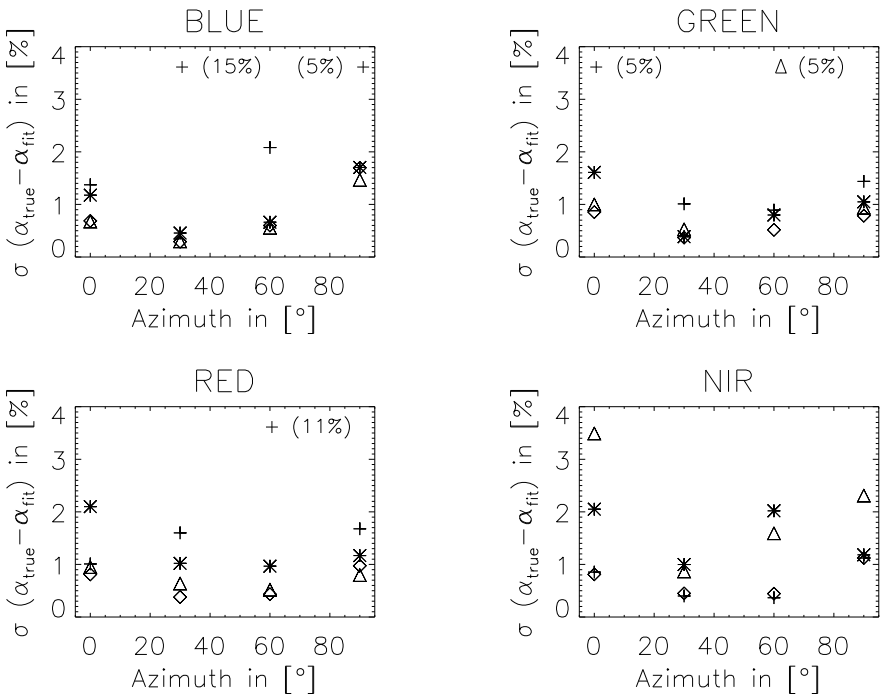

Figure 4: Standard deviation of the albedo error for a version of the CSAR BRF without parameter limits but an atmospheric transmission term correction as a function of surface cover (see section 5).

5.4 Algorithm with Atmospheric Pre-Correction

Since the CSAR model has been developed to model surface BRFs rather than TOA BRFs, it was suggested (Diner, 1995) that one could subtract the Rayleigh scattered part of the path radiance from the measured BRFs and thus get closer to a surface BRF. We took this suggestion and ran JMRT for a dark surface with no aerosol content to calculate the Rayleigh scattered path radiance which we converted in a BRF: $BRF_{Rayleigh}$. Since the direct radiance from the ground is also attenuated in the atmosphere we just multiplied the CSAR BRF with a mean transmission factor $T_c = \exp(-\tau_c/\mu_i)$ where $\tau_c = [.24, .094, .043, .015]$. The modified BRF slice is then:

$$BRF_4(\theta_i, \phi_i) = BRF_{CSAR}(\theta_i, \phi_i; \varrho_0, \kappa, \Theta_0) \exp(-\tau_c/\mu_i) - BRF_{Rayleigh}(\theta_i, \phi_i),\ i = 1, 2, 3, \ldots, 9;\ c = 1, 2, 3, 4 \quad (9)$$

and the albedo is given by the sum of:

$$\alpha_0 = Albedo(BRF_{CSAR,fit}(\theta_i, \phi_j) \exp(-\tau_c/\mu_i)) + Albedo(BRF_{Rayleigh}(\theta_i, \phi_j)),$$
$$i = 1, 2, 3, \ldots, N_\theta;\ j = 1, 2, 3, \ldots, N_\phi;\ c = 1, 2, 3, 4, \quad (10)$$

where $BRF_{CSAR,fit}(\theta_i, \phi_j)$ is the hemispherical BRF computed from the best fit of the CSAR parameters to the BRF slice $BRF_4(\theta_i, \phi_i)$. The albedo is calculated using eq.(4). The results (Figure 5) show an improvement especially for the blue channel where most albedo errors lie below 1%. We again see larger albedo errors for bright surfaces (snow/ice in channels 2, 3 and 4; vegetation in the NIR). For some reason water is also a problem for some azimuthal angles in the green and red. Thus it seems that this approach works well for the blue where the Rayleigh scattering contributes a lot to the TOA BRF but that this approach causes numerical problems for the other channel. From our experience using the 2-parameter constrained BRF_2 it seems that one should use this last approach with an atmospheric pre-correction and limit the parameters to α_0' and κ'.

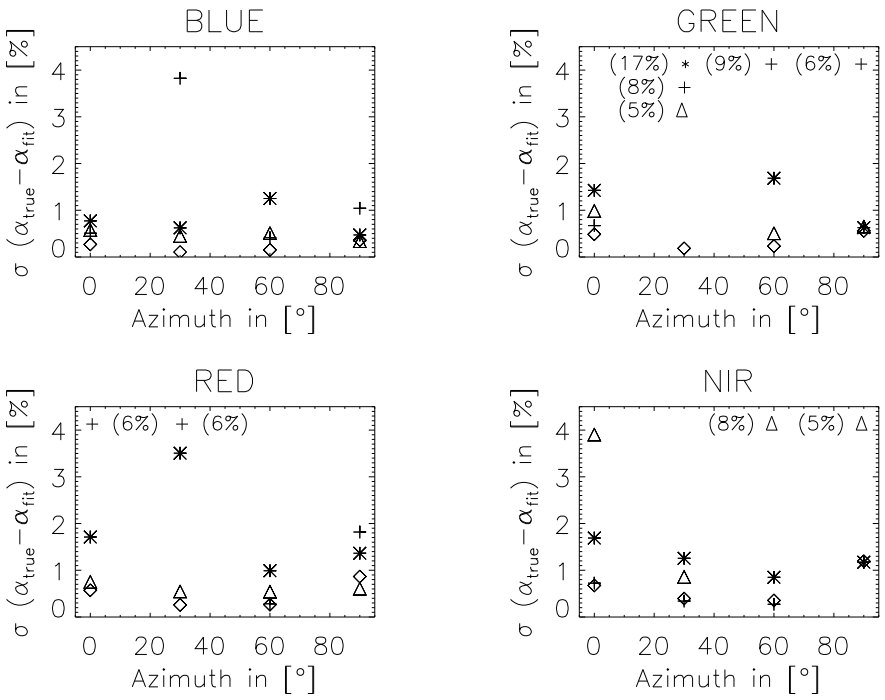

Figure 5: Standard deviation of the albedo error for unlimited parameter version of the CSAR BRF with atmospheric pre-correction as a function of surface cover (see section 5).

6 Conclusions

We find that for most cases our albedo error will be less than 1% in the visible and less than 1.5% in the NIR which is a significant advancement of the state-of-the-art for global change research goals. In contrast, if only nadir measurements are used the albedo error is about 5 % in the visible and 10 % in the NIR. More work is however needed to make this approach robustly work for all surfaces and atmospheric conditions. Another problem is to perform the inversion more rapidly and flag pixels for which the model did not fit very well. This approach lends itself to calculate the hemispherical BRF field over any region of the Earth. We will next investigate how the CSAR parameters vary as a function of sun angle. If we find that there is a diurnal smooth trajectory for a parameter with sun angle we could use this to predict the TOA clear sky albedo at times of the day other than those at which MISR observed it and integrate the TOA albedo over the period of a day. Using MISR derived atmospheric properties we could refine our atmospheric pre-correction scheme and directly retrieve surface BRF-CSAR parameters and potentially compute the surface albedo.

7 Acknowledgments

This work was supported by the Multi-angle Imaging Spectro Radiometer (MISR) project through a contract from NASA/JPL. We recognize the significant contributions by Dr. Carmen Tornow (DLR, Berlin), Dr. Veronique Carrére (JRC, Ispra) and Heather Stephens (LANL) and Kerstin Lippert (LANL and DLR, Berlin).

8 References

Abreu L.W., Chetwynd J.H, Anderson G.P. and Kimball L.M., 1995, MODTRAN 3 Scientific Report. Draft Preprint, Geophysics Laboratory, Air Force Command, US Air Force, Hanscom AFB, MA, USA.

Borel C.C., Tornow C. and Gerstl S.A.W., 1995, MISR quarterly report, July, (available on request from C. Borel).

Diner D.J., Clothiaux E., Conel J.E., Davies R., Di Girolamo L., Muller J.-P., Varnai T. and Wenkert D., 1994, MISR Level 2 Algorithm Theoretical Product: TOA/Cloud Product, JPL Report D-11399, March 3.

Diner D., 1995, personal communication.

Goel N.S., 1988, Models of Vegetation Canopy Reflectance and Their Use in Estimation of Biophysical Parameters from Reflectance Data, Remote Sensing Reviews, 4:1:1-222.

Kimes D.S. and Sellers P.J., 1985, Inferring hemispherical reflectance of the earth's surface for global energy budgets from remotely sensed nadir or directional radiance values, Remote Sens. Environ., 18, pp.205-223.

King M.D. and Harshvardhan, 1986, Comparative accuracy of selected multiple scattering approximations, J. Atmos. Sci., 43:8, pp.784-801.

Koepke P., Kriebel K.T. and Dietrich B., 1985, The effect of surface reflection function and of atmospheric parameters on the short wave radiation budget, Adv. Space Res., 9:6, pp.351-354.

Li S., Wan Z. and Dozier J., 1985, A component decomposition model for evaluating atmospheric effects in remote sensing, J. Electromag. Waves.

Martonchik J.V., 1994, personal communication.

Nicodemus F.E., Richmond J.C., Hsia J.J., Ginsberg I.W. and Limperis T., 1977, Geometrical Considerations and Nomenclature for Reflectance, Washington, D.C.: NBS Monograph 160, National Bureau of Standards, Dept. of Commerce, p.52.

Tornow C., Borel C.C. and Gerstl S.A.W., 1995, MISR quarterly report, September, (available on request from C. Borel).

Rahman H., Verstraete M.M. and Pinty B., 1993, Coupled Surface-Atmosphere Reflectance (CSAR) Model (parts 1 and 2), JGR, 98:D11:20,779-20,789 and 98:D11:20,791-20,801.

Vermote E., Tanré D., Deuzé J.L., Herman M. and Morcette J.J., 1994, Second Simulation of the Satellite Signal in the Solar Spectrum, 6S User Guide Version n 0, NASA-Goddard Space Flight Center, Greenbelt, USA, P 182.